Materials & Design 248 (2024) 113485

Contents lists available at ScienceDirect

Materials & Design

journal homepage: www.elsevier.com/locate/matdes

Orientation matters: Assessing the cyclic deformation behaviour of laser powder bed fusion Ti-6Al-4V

Jieming S. Zhang [a,*], Yun Deng [a], Huifang Liu [b], Yuanbo T. Tang [a,c], Andrew Lui [a], Patrick S. Grant [a], Enrique Alabort [d], Roger C. Reed [a,b], Alan C.F. Cocks [b]

[a] Department of Materials, University of Oxford, Parks Road, Oxford, OX1 3PH, United Kingdom
[b] Department of Engineering Science, University of Oxford, Parks Road, Oxford, OX1 3PJ, United Kingdom
[c] School of Metallurgy and Materials, University of Birmingham, Edgbaston, Birmingham, B15 2TT, United Kingdom
[d] Alloyed Ltd, Unit 15, Oxford Industrial Park, Yarnton, OX5 1QU, United Kingdom

ARTICLE INFO

Keywords:
Titanium
Laser powder bed fusion
Fatigue
Orientation-dependency
X-ray computed tomography

ABSTRACT

The orientation dependency of the fatigue behaviour of laser powder bed fusion Ti-6Al-4V has been analyzed and rationalized. Seven build orientations relative to the build plate have been studied. The 75° specimen demonstrates the highest fatigue life owing to the optimal surface quality and low proportions of grains near-parallel to the loading direction. When the build orientation is 30° or below, only defects on the downward-facing surface serve as the fatigue crack initiation sites as a result of the poor surface quality. Beyond 45°, cracks begin to initiate from the otherward-facing surface owing to the reduced variation in R_a across the sample surface. The large variation in the size and number of pore clusters near the initiation site governs the highest fatigue scatter of the 75° specimen whereas the difference in crack initiation sites of the 45° specimen results in the large difference in fatigue life. Our results demonstrate that the orientation effect is a critical factor to consider for the design of fatigue-tolerant intricate components.

1. Introduction

Advanced manufacturing, particularly metal additive manufacturing (AM), stands as the cornerstone for the fourth industrial revolution – also known as the "Industrial 4.0" [1–3]. From biomedical spinal implants to automotive engine parts, its ability to fabricate complex structures at high geometrical precision opens the door for the design of lightweight and multifunctional components [4–6]. Collective wisdom in the realm of topological optimisation entails elements to be printed in different build orientations [7–9]. However, a strong orientation-dependent mechanical property of the printed elements has been found i.e. vertical struts exhibit different properties from the horizontal struts [7,9]. This is due to the different local thermal history that gives rise to the formation of structural inhomogeneities such as surface defects, pores, and inhomogeneous microstructure [7,9]. So far, the orientation effect has been widely assessed for the quasi-static mechanical behaviour of AM materials [7,10,11]. The significance of the inhomogeneity on the mechanical durability, particularly the fatigue behaviour, of the component is largely underexplored, which gives rise to severe ramifications in practice and hinders the certification of the AM process [12–14]. Hence, in order to capitalize on the tremendous opportunities that AM offers, the orientation dependency of the fatigue behaviour must be elucidated.

Here, Ti-6Al-4V alloys are employed for their broad applications in both aerospace and biomedical industries [7,14,15]. We have chosen laser powder bed fusion (L-PBF) to fabricate the alloy since the technique often has a higher spatial resolution than the other AM techniques such as electron beam melting (EBM) and direct energy deposition (DED) and the parts produced by L-PBF usually exhibit better surface finish than the EBM and DED counterparts [16–18]. Owing to the rapid cooling rate of the process ($10^4 - 10^6$ K/s), the microstructure of Ti-6Al-4V alloy made by L-PBF consists of α' martensitic laths resulting from the decomposition of prior-β grains during the solidification process [17,19]. After heat treatment, the microstructure is coarsened, which yields the transformation of the α' martensite into α laths [17,20]. Moreover, the thermal cycling intrinsic to the process can induce the formation of defects such as surface irregularity and porosity in Ti-6Al-4V alloys [14,21]. The presence of these defects can be detrimental to the fatigue behaviour of the alloy [12,14]. Therefore, they are considered in this study.

* Corresponding author.
E-mail address: jieming.zhang@materials.ox.ac.uk (J.S. Zhang).

https://doi.org/10.1016/j.matdes.2024.113485
Received 23 September 2024; Received in revised form 3 November 2024; Accepted 21 November 2024
Available online 26 November 2024

So, how does printing orientation influence the fatigue behaviour of AM materials? Existing research has focused on machined specimens with the effect of surface roughness often neglected or not emphasised [22–26]. However, machining is not applicable to complex structures in service conditions, which calls into question the relevance of this research to practical engineering components. On the other hand, studies on as-built specimens have usually been restricted to three orientations: 0°, 45°, and 90° with respect to the build plate [27–30]. The broad rule-of-thumb so far is that the 90° specimen demonstrates the highest fatigue strength as a result of the optimal surface finish. But this oversimplifies the situation. Intricate components often require a multitude of printing orientations. An attempt to assess the fatigue behaviour of specimens printed in five different orientations was described in [8]. Yet, the study focused on one test condition of 600 MPa maximum stress, and adopted both rectangular and cylindrical geometries in specimen design, which limited our ability to derive further insight into the factors that influence the fatigue behaviour [8]. The synergistic effects of microstructure, surface defects, and porosity during the fatigue fracture process need further study.

The present study was initiated with the above in mind. Ti-6Al-4V specimens were designed and printed in seven build orientations. The gauge diameter of the specimen was chosen to match the strut thicknesses of many engineering components, including biomedical implants and cooling channels [17,16]. The overarching goal of this work is to rationalize the variation in the deformation and fatigue behaviour of AM materials in the as-built conditions as a function of the build orientation, such that the orientation effect can be leveraged to inform the fatigue response of complex structures in practice. We determined the fatigue life of AM specimens between 5×10^3 and 10^6 cycles to inform the behaviour of metallic lattices. The 75° specimen exhibited the optimal fatigue resistance among all the specimens. A combination of high-resolution microscopy and X-ray computed tomography was employed to examine structural inhomogeneities, which allows the major factors relevant to the fatigue properties to be quantified. We then probed the fracture surface to shed light on the cyclic deformation process of L-PBF Ti-6Al-4V. It was confirmed that surface defects served as the fatigue initiation sites for all the tested specimens, indicating surface roughness is the primary factor governing the fatigue performance of L-PBF Ti-6Al-4V. These findings can pave the pathway for designing AM parts against the presence of structural inhomogeneities.

2. Methods

2.1. Design of experimentation

In order to study the effect of printing orientations on the elastic, plastic, and fatigue properties, samples were printed in seven different orientations relative to the build plate: 0°, 15°, 30°, 45°, 60°, 75°, and 90°, as shown in Fig. 1(A). All samples were designed with a gauge length of 5.2 mm and a gauge diameter of 1.3 mm.

2.2. Processing by laser powder bed fusion

A Renishaw AM400 machine (Renishaw plc, UK) with a modulated 200 W ytterbium fibre laser was employed to produce the tensile samples. Electrode induction-melted gas atomised Ti-6Al-4V powders were fed into the machine. Table 1 details the processing parameters used in this study. The processing parameters were optimised to obtain fully dense samples through single-track experiments followed by the Archimedes density measurements. The detail of how the optimal processing parameters were identified was described in our previous work [31]. A stripe hatching laser scan path pattern with a 67° rotation between each layer was adopted (Fig. 1(B)). Two contour passes were performed near the free surfaces after each layer to achieve an optimal surface quality. We used hatch parameters for the internal pass and border parameters for the external pass (Fig. 1(C)).

Table 1
Processing parameters used for the manufacturing of tensile samples.

Ti-6Al-4V	Hatch Parameters	Border Parameters
Layer Thickness	30 µm	30 µm
Laser Power	200 W	100 W
Laser Scan Speed	0.786 m/s	0.750 m/s
Point Distance	55 µm	45 µm
Hatch Distance	65 µm	65 µm
Exposure Time	50 µs	40 µs
Spot Size (Radius)	35 µm	35 µm

For specimens below 30°, support structures were added. The specimens were printed at nine equally spaced locations on a 250 mm × 250 mm build plate (Fig. 1(D)). Each sample consisted of a downward-facing surface facing toward the build plate and an otherward-facing surface facing in the other direction (Fig. 1(E)). In the L-PBF process, the downward-facing surface was usually printed on top of the loose powders whereas the otherward-facing surface was printed on top of the solid part [32,33]. After the fabrication, the support structures were manually removed from the samples below 30° with special care. All the samples were heat treated at 800°C for 4 hours in a vacuum furnace and then sandblasted using safti grit at 2 bar.

2.3. Assessment of static & fatigue behaviour

The mechanical behaviour at room temperature was examined using an Instron ElectroPuls E10k system with a 10kN load cell. Uniaxial tensile tests were conducted under displacement rate control at a strain rate of 2×10^{-3} s^{-1}. The macroscopic strain of the sample was measured on a 5.2 mm gauge length using a non-contact iMetrum video extensometry system. We performed 21 uniaxial tensile tests in total.

Tensile fatigue tests were performed under load control at a frequency of 30 Hz and an R ratio of 0.1. Specimens were tested at maximum applied stresses of 600 MPa, 500 MPa, and 400 MPa. Three tests were performed at each applied stress – a total of 63 fatigue tests were conducted. All specimens were tested until rupture.

2.4. Characterization by electron microscopy

Microstructures were characterized using a Zeiss Merlin field emission gun scanning electron microscope (FEG-SEM) equipped with a Bruker electron backscatter diffraction (EBSD) detector. Surfaces parallel to the build direction were examined. Scans were performed at a 20 kV accelerating voltage and a 20 nA current. To evaluate the α lath thickness distribution, the diffraction patterns were acquired at 400 × 300 resolution with a step size of 0.22 µm. To analyze the α lath Schmid factor and reconstruct prior-β grains, the diffraction patterns were collected at 400 × 300 resolution with a step size of 0.55 µm.

Fracture surfaces of the samples after fatigue tests were examined using a JEOL 6500F FEG-SEM. Fatigue crack initiation sites were identified to determine the failure mechanisms.

2.5. X-ray computed tomography

An ImageiX CT system (North Star Imaging Inc., Minnesota, USA) was employed to conduct the X-ray computed tomography of the tensile samples. The gauge sections of the samples were detected for the quantification of surface quality and porosity. During the scan, each sample was positioned 25.5 mm in front of the tungsten transmission target X-ray source filtered by a Cu foil of 0.95 mm thickness. The scan conditions were: 140 kV tube voltage, 71 μA tube current, 5 µm focal spot size, and 1 Hz frame rate. We set the isotropic voxel size to be 4.7 µm and thus any feature smaller than 14.1 µm cannot be resolved [34]. Reconstruction of the projection images was performed following a filtered back Projection algorithm in the efX-ct software (version 1.9.5.12, North Star

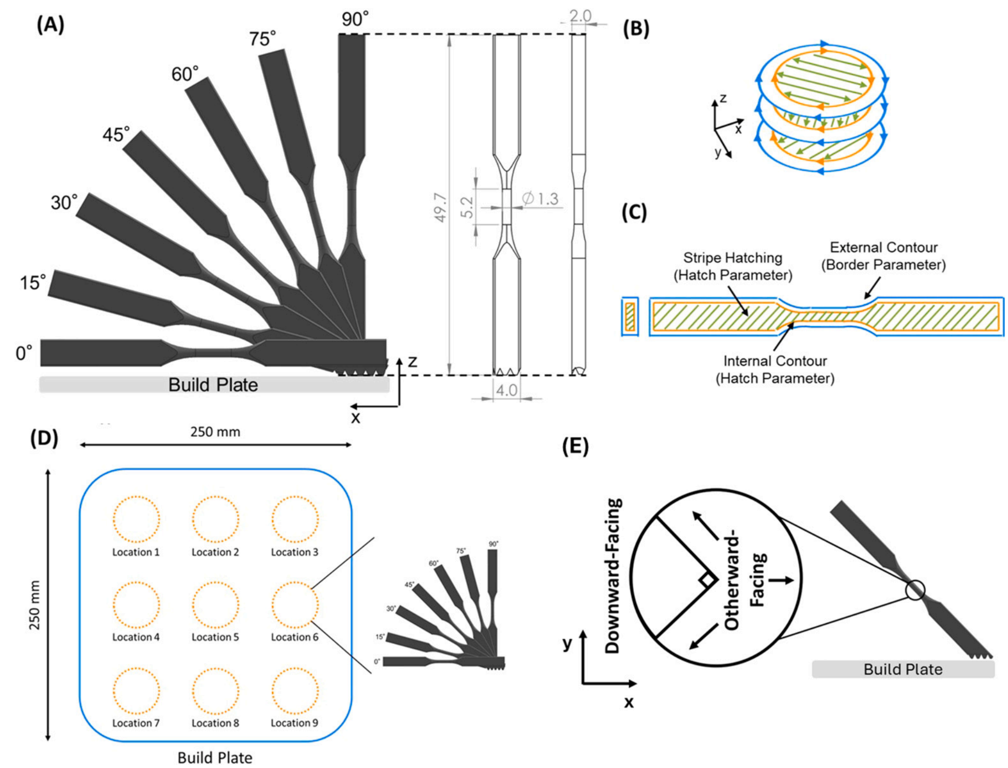

Fig. 1. (A) Geometries of the 7 tensile specimens used in this study. Schematic illustrations of (B) laser path along different consecutive layers, (C) laser path along each cross-sectional plane, (D) specimen distribution on the build plate, and (E) downward-facing and otherward-facing surfaces of the specimen.

Imaging Inc., Minnesota, USA). The data was analyzed using Avizo 9.7 software. Segmentation of the solid parts was performed using Otsu's method [35].

3. Results

3.1. Quasi-static mechanical behaviour

The quasi-static mechanical performance of the 7 specimens is presented in Fig. 2(A). The variation of yield strength, ultimate tensile strength, and fracture strain with build orientation is shown in Fig. 2(B). All the specimens demonstrate average yield strength between 850 MPa and 950 MPa and ultimate tensile strength between 950 MPa and 1050 MPa, which are consistent with the values in the previous reports on L-PBF Ti-6Al-4V [17,36]. Both yield strength and ultimate tensile strength exhibit an increase when the build orientation increases from 0° to 15°, a drop from 15° to 75°, and a final increase from 75° to 90°. The 15° specimen demonstrates an 84 MPa higher yield strength and 53 MPa higher ultimate tensile strength on average than the 75° specimen. On the other hand, there is an inversion of the tendency with the fracture strain. The 15° specimen shows around 9% lower average fracture strain than the 75° specimen. This orientation dependency is further discussed in Sec. 4.1.

3.2. Fatigue behaviour

Following the quasi-static results above, the fatigue response of samples with different build orientations is illustrated in Fig. 3(A). When $\sigma_{\max} = 600$ MPa, all the specimens fail between 5×10^3 and 3×10^4 cycles. At $\sigma_{\max} = 500$ MPa, the cycles to failure are largely in the range of 10^4 and 1.5×10^5 cycles. When the $\sigma_{\max}$ drops to 400 MPa, the cycles to failure are mostly between 2×10^4 and 2×10^5 cycles. These values are in the range of the previous results on the as-built L-PBF Ti-6Al-4V [37,17,30].

The variation in cycles to failure with the build orientation is shown in Fig. 3(B). At all applied stresses, cycles to failure generally increase as the build orientation increases and a final drop in cycles to failure is observed for the 90° specimen. The only exception is at $\sigma_{\max} = 500$ MPa, where the drop starts from the 75° specimen.

The scatter in fatigue life at each applied stress is evaluated by the coefficient of variation. Results are shown in Fig. 3(C) and the numerical values are provided in Supplementary Table 1. The 75° specimen shows the highest fatigue scatter at $\sigma_{\max} = 500$ MPa (74%) followed by the 45° specimen at $\sigma_{\max} = 500$ MPa (63%). No significant correlation between the fatigue scatter and applied stress can be observed. The orientation dependency of the fatigue properties is rationalized in Sec. 4.3.

3.3. Microstructural characterization

Fig. 4 displays the EBSD maps of the 7 specimens under study. All microstructures are composed of more than 95% thin α laths organized in bundles inherited from the prior-β grains. For 0° specimen, the prior-β grains seem to be perpendicular to the longitudinal direction of the specimen. As the specimen is more vertically built, the prior-β grains seem to be more aligned with the longitudinal direction of the specimen. The α lath thickness is similar across all the specimens and the detailed analysis is illustrated in Supplementary Sec. 2. The contour pole figure confirms $\{0001\}$ has the strongest texture among the three plane families $\{0001\}$ $\{\bar{1}100\}$ and $\{\bar{1}2\bar{1}0\}$ in α microstructure with respect to the x-z plane of Fig. 1(B) (Fig. 5(A)). The quantification of the texture strength in Fig. 5(B) shows all the specimens exhibit α texture indices below 2.5, which suggests the α microstructure of L-PBF Ti-6Al-4V is weakly textured [38,7]. Additionally, the variation in texture strength of different specimens is minimal.

We reconstruct the prior-β grains from the descendant α lath structure using the MTEX 5.8.2 tool box following the transformation indicated in Figure 4 [39]. Each α lath is analyzed together with the

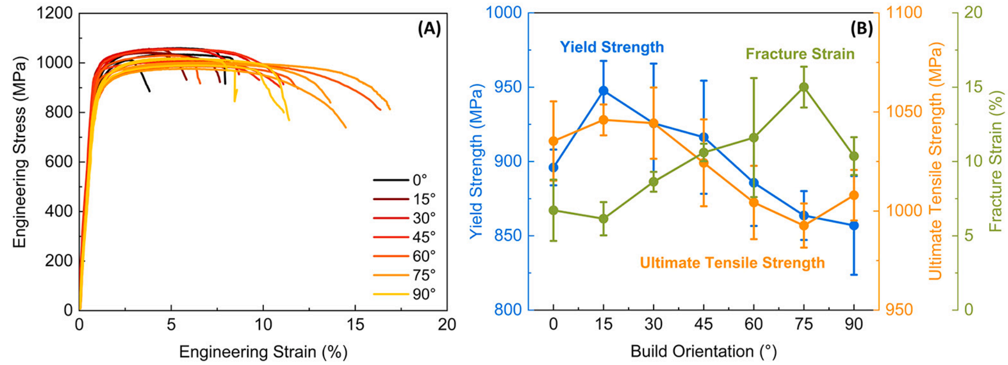

Fig. 2. (A) Engineering stress-strain curves of AM Ti-6Al-4V at a strain rate of 2×10^{-3} s^{-1}. (B) Yield strength, ultimate tensile strength, and fracture strain vs. build orientation of the 7 specimens under study. Error bars represent the standard deviation from 3 repetitions.

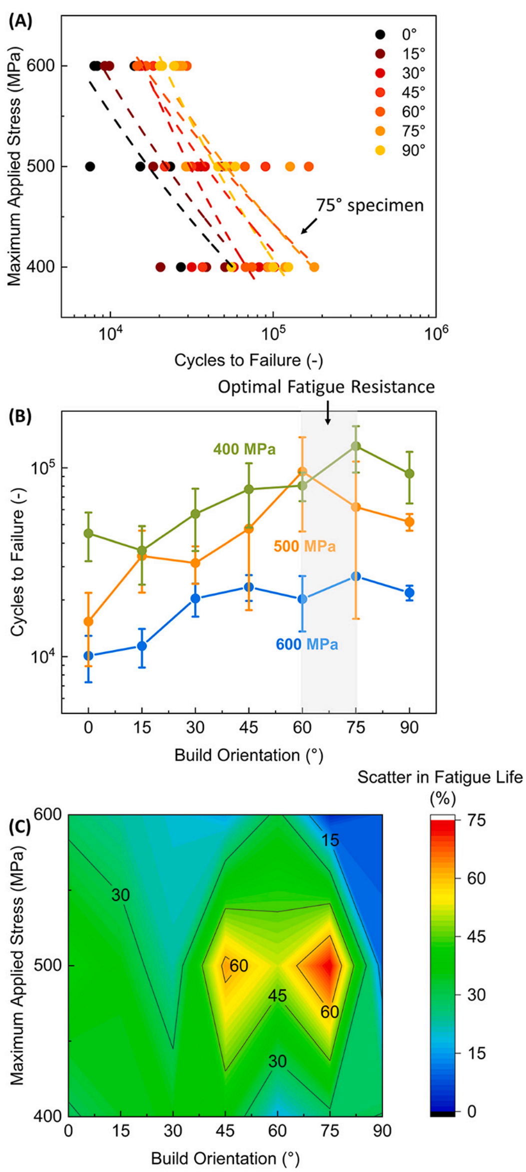

Fig. 3. (A) Maximum applied stress vs. cycles to failure for the specimens built at different orientations. Three measurements are performed at each condition. (B) Cycles to failure vs. build orientation for the specimens manufactured in this work. Error bars represent the standard deviation from 3 repetitions. (C) Calculated map of scatter in fatigue life as a function of build orientation and maximum applied stress for the specimens built at seven orientations.

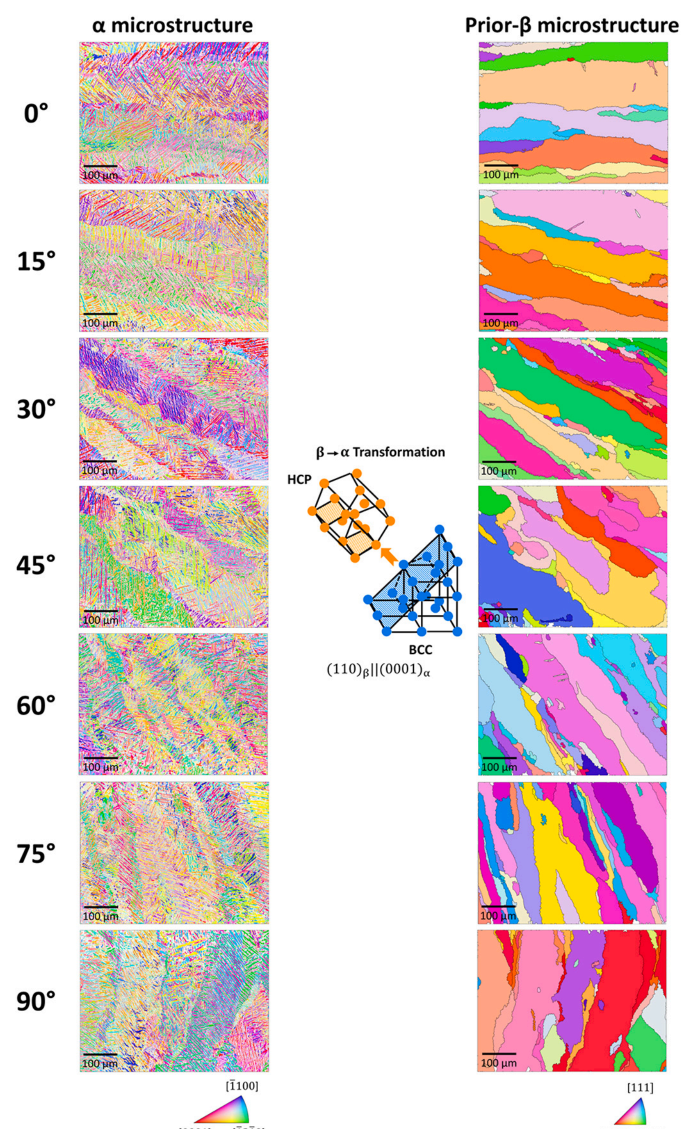

Fig. 4. Longitudinal EBSD maps of the α lath and the associated reconstructed prior-β microstructure of the 7 specimens under study.

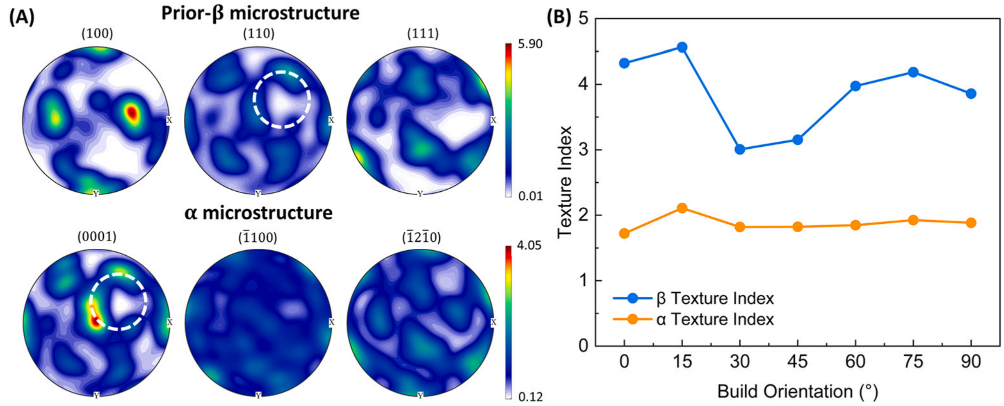

Fig. 5. (A) Contour pole figures of the α and prior-β microstructure of the 90° specimen. The texture rings confirm the $\beta \rightarrow \alpha$ transformation during the solidification process. (B) Texture index vs. build orientation for all the specimens.

neighbouring α laths to find the suitable prior-β grain based on the following Burgers orientation relationship:

$$(110)_\beta//(0001)_\alpha, [111]_\beta//[11\bar{2}0]_\alpha \tag{1}$$

If the neighbouring laths are of the same prior-β orientation, these laths are associated with the same prior-β grain. The process iterates across the whole set of laths.

As shown in Fig. 4, columnar grains along the build orientation can be observed. The remelting and resolidification of each layer give rise to epitaxial grain growth opposing the maximum temperature gradient [7,17]. When the 0° specimen is printed, the maximum temperature gradient is roughly along the z-direction (see Fig. 1(A)), which gives columnar grains perpendicular to the longitudinal direction of the specimen. As the build orientation increases, the maximum temperature gradient is always along the z-direction, but the longitudinal direction of the specimen becomes closer to the z-direction, and thus the columnar grains become more aligned with the longitudinal direction. The contour pole figure of Fig. 5(A) exhibits the texture strength for the three plane families $\{100\}$ $\{110\}$ and $\{111\}$ in the prior-β microstructure with respect to the x-z plane of Fig. 1(B). In all the specimens, the $\{100\}$ texture component is the strongest [14]. The crystallographic nature of the $\beta \rightarrow \alpha$ transformation is also clearly revealed by the transfer of texture. The pole figure shows the Burgers orientation relationship between the two phases – $(110)_\beta//(0001)_\alpha$. The same texture ring can be observed along both $(110)_\beta$ and $(0001)_\alpha$, which confirms the success of our reconstruction.

Unlike the α microstructure, the prior-β grains demonstrate significant variations in texture strength across different specimens. The β texture index of the 15° specimen is more than 50% higher than that of the 30° specimen. Nevertheless, the martensitic transformation during the solidification process deteriorates the variant selection in Ti-6Al-4V alloys, resulting in a weakly textured α lath microstructure [40–42].

3.4. Surface roughness

The surface profiles of different specimens were evaluated using the XCT data. The downward-facing surface of the specimen that faces toward the build plate was usually found to demonstrate a higher surface roughness than the otherward-facing surface since the downward-facing surface was printed on top of the loose powders in the L-PBF process [13,32]. Hence, the surface roughness of downward-facing and otherward-facing surfaces was evaluated separately. Cross-sectional images on both the sagittal and coronal planes were extracted from the tomography data. After binarization, the specimen edges were detected and analyzed using Image-J as shown in Fig. 6(A). The surface roughness (R_a) for each line profile was then computed. R_a is one of the most commonly used parameters to assess the surface quality of AM parts [13,17]. Results are shown in Fig. 6(B). Apart from the 90° specimen, the downward-facing surfaces of all other specimens were confirmed to exhibit higher surface roughness than the otherward-facing surfaces as a result of dross formation [32,33]. When the laser enters the overhang regions, the loose powders underneath the downward-facing surface hinder heat dissipation owing to the low thermal conductivity, resulting in the collapse of the quasi-steady state melt pool [32,33]. The excessive heat then leads to a keyhole-like melt mode, which causes a drilling effect [32,33].

Moreover, the difference in surface roughness between the downward-facing and otherward-facing surfaces is significantly reduced when the build orientation increases from 0° to 75°. This can be attributed to the less pronounced dross formation as the overhang regions become smaller [33]. Additionally, no significant difference in surface roughness can be found between the 30° and 45° specimens. The presence of support structures transfers the heat from the samples to the build plate, which improves the melt pool stability and reduces dross formation [43–45]. However, after the support structure is removed, connection marks are introduced into the sample surfaces deteriorating the surface quality [46,47]. The combination of these two factors gives rise to comparable surface roughness between the two specimens.

3.5. Processing-induced porosity

The presence of porosity was also identified and quantified using the XCT data (Fig. 7(A)). Fig. 7(B) shows the spatial distributions of the pores in the x-y plane of the 0°, 30°, and 90° specimens. In the 0° sample, the pores are mostly near the downward-facing surface. In the 30° sample, they start to populate near the otherward-facing surface. In the 90° sample, the pores are uniformly distributed close to the entire sample surface.

We further confirm this statement by the quantification in Fig. 7(C), where the distribution of pores in the x-y plane is evaluated across the entire gauge length. The downward-facing direction is set at a polar angle of 180°. In the 0° sample, more than 60% of the pores are found to be close to the downward-facing surface. This value decreases to 38% in the 30° sample. In the 90° sample, only 20% of the pores are adjacent to the downward-facing surface, which is similar to the pore populations adjacent to other-oriented surfaces within the specimen. The variation in the spatial distribution of the pores can be explained by the pore formation mechanisms [32,33]. When the build orientation is 0°, the low thermal conductivity of the loose powders below the downward-facing surface results in low heat dissipation [32,33]. The heat accumulation can lead to the formation of unstable melt pools, which gives rise to gas entrapment and the formation of gas pores [32,33]. As the build orientation increases, the overhang regions reduce and there is less heat accumulation below the downward-facing surface and thus fewer gas pores are generated [32,33].

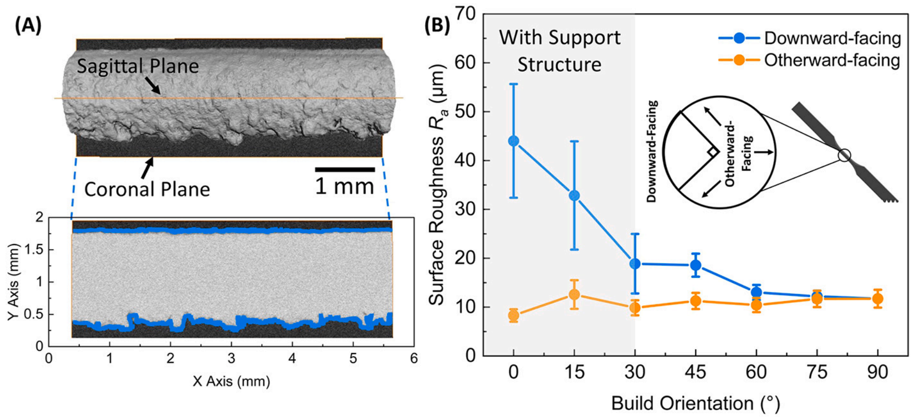

Fig. 6. (A) An example of the surface roughness (R_a) measurement on the 0° specimen. (B) Downward-facing and otherward-facing surface roughness (R_a) as a function of the build orientation. Error bars represent the standard deviation from 3 repetitions.

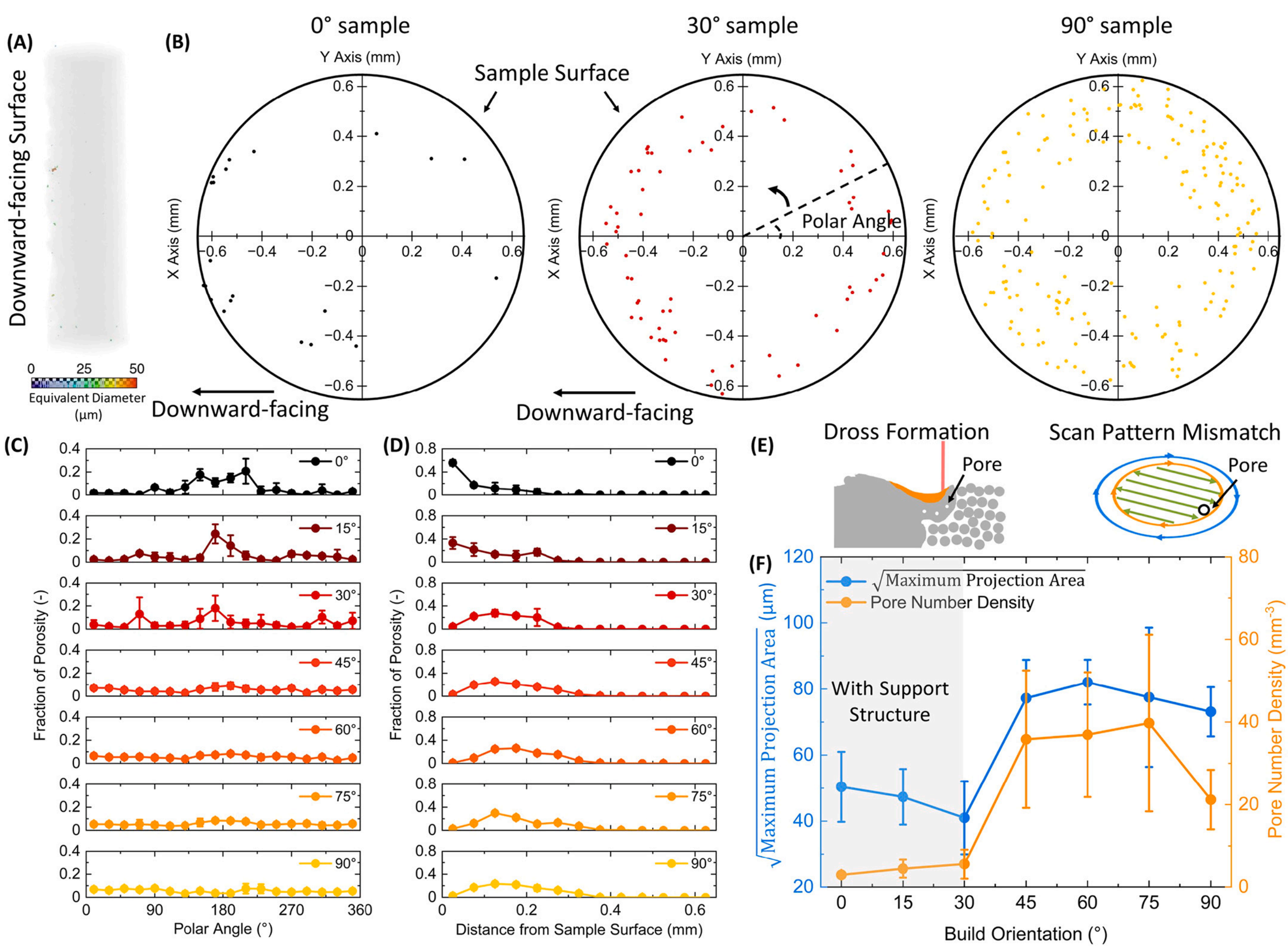

Fig. 7. (A) 3D rendered XCT images of a 0° sample and pores inside the sample. (B) Projection view of the porosity distribution along the build direction in the 0°, 30°, and 90° samples. (C) Quantification of porosity in the x-y plane across the entire sample gauge length as a function of the polar angle. The downward-facing direction is set at a polar angle of 180°. (D) Fraction of porosity against the distance from the sample surface. (E) Schematic illustration of the pore formation mechanisms. (F) $\sqrt{\text{Maximum Projection Area}}$, $\sqrt{A_{\text{P, max}}}$, and number of pores per unit volume as a function of the build orientation. The maximum projection area is determined by evaluating the maximum cross-sectional area of each pore in the x-y plane, and all the pores in the gauge volume are considered.

In addition, the distances of the pores from the sample surface are depicted in Fig. 7(D). In the 0° sample, more than 70% of the pores are within 0.1 mm of the sample surface. When the build orientation increases, the pores start to distribute more towards the centre of the sample. In the 90° sample, more than 80% of the pores are found to be between 0.1 mm and 0.4 mm away from the sample surface. This suggests the pore formation mechanisms are different in different specimens (Fig. 7(E)). As discussed above, the pores are mainly induced by dross formation in the 0° sample. When the samples are built more vertically, the majority of the pores are formed due to the mismatch between the strip hatching and contour scan patterns and the gaps between contour passes [48–50].

The size and number density of the pores are also important factors to consider for the fatigue performance of AM components [51,52]. The size of the pores is given by the Murakami parameter $\sqrt{A_P}$ where A_P is the projection area in the plane normal to the loading direction, and their number density is characterized by the number of pores per unit volume [51,53]. The maximum projection area is evaluated by determining the maximum cross-sectional area of each pore in the x-y plane and all the pores in the gauge volume are considered regardless of the locations and shapes [51,53]. Results are shown in Fig. 7(F). When the build orientation is 30° or below, the maximum $\sqrt{A_P}$ of the pores within all the specimens is lower than 50 μm on average, and the average number density of the pores is smaller than 6 mm^{-3}. As the build orientation increases to 45° or above, the pores have maximum $\sqrt{A_P}$ larger than 70 μm on average, and a number density higher than 20 mm^{-3}. The substantial difference in the porosity level results from the use of support structures when the build orientation is 30° or below [43]. These support structures can facilitate the heat transfer between samples and build plate, lowering the thermal gradient within the samples, which enables more pores to escape into the atmosphere [43–45].

Even though there are also reports suggesting the Murakami parameter may not be strongly correlated with the fatigue performance of Ti-6Al-4V alloy [54], the measurements here can provide an indication of the pore size in the printed specimens and how the maximum pore size varies with the build orientation.

4. Discussion

The above results provide quantitative evidence of the strong orientation dependency of the surface quality, processing-induced porosity, and microstructural development of AM Ti-6Al-4V. However, these results warrant further rationalization and deeper understanding can be gained via more detailed analysis.

4.1. Rationalization of the variation in tensile properties

AM often introduces geometrical deviations and porosity in the printed parts, which may reduce the effective loading area resulting in lower yield strength and ultimate tensile strength [55,56]. To evaluate the effective loading area, we measure the minimum cross sectional area of a specimen from the XCT data [16,55]. Fig. 8(B) presents the results normalized by the designed area. The effective loading area generally decreases as the samples are built more vertically. The 0° specimen demonstrates 6.8% higher effective loading area compared to the 90° specimen.

We then proceed by correcting the tensile properties with the effective loading area. Results are shown in Fig. 8(C). The corrected values of yield strength and ultimate tensile strength exhibit similar trends to the uncorrected values. The 15° specimen has a 64 MPa higher average yield strength than the 75° specimen while the 30° specimen has a 49 MPa higher average ultimate tensile strength than the 75° specimen. L-PBF Ti-6Al-4V is known to lack work hardenability due to the high dislocation density after processing [57,36]. Hence, the variation in both properties can be attributed to the slip behaviour of α grains.

In hcp crystals, there are five different families of slip systems, namely the basal $\langle a \rangle$, prismatic $\langle a \rangle$, pyramidal $\langle a \rangle$, first order pyramidal $\langle a+c \rangle$, and second order pyramidal $\langle a+c \rangle$ slip systems with 30 possible slip systems in total, as shown in Fig. 9(A). Among them, basal $\langle a \rangle$, prismatic $\langle a \rangle$, and first order pyramidal $\langle a+c \rangle$ are the main operating deformation systems at room temperature [58–60]. When grains start to deform, the shear stress acting in the slip direction on the slip plane needs to reach a critical value to activate the slip activity and the critical shear stress τ_C can be evaluated following Schmid's law:

$$\tau_C = \sigma_a m \tag{2}$$

where σ_a is the applied normal stress to activate the slip activity and m is the Schmid factor.

Based on this theory, grains with high Schmid factors (0.4-0.5) require a relatively low applied stress to trigger dislocation motion [36,61]. Hence, we evaluate the proportion of grains with high Schmid factors in each specimen and the results are shown in Fig. 9(B). Among the three families of slip systems, the trend in how the proportion of grains with high Schmid factors for the prismatic $\langle a \rangle$ slip system varies with build orientation is consistent with how the yield strength and ultimate tensile strength changes with orientation (see Fig. 8(B)). This suggests the prismatic $\langle a \rangle$ slip system governs the plastic deformation of the specimens. This is consistent with previous literature [36,62,63]. During the plastic deformation of L-PBF Ti-6Al-4V, strain localization starts from the α grains with high prismatic Schmid factors, owing to the lower value of τ_c for the prismatic $\langle a \rangle$ slip system, compared to the other slip systems.

Also, when there are more grains with high prismatic Schmid factors, more slip activity is triggered during the plastic deformation. The increased amount of dislocation motion enables the specimen to undergo more plastic deformation resulting in a higher fracture strain of the specimen [64]. This is also consistent with the experimental trend indicated in Fig. 2(B).

4.2. Fatigue fracture behaviour

The fracture surface morphology of a sample after fatigue testing is shown in Fig. 10. Three steps in the fatigue fracture process are clearly revealed. In region I, surface defects serve as the fatigue crack initiation sites. Relatively flat surrounding regions can be observed, which suggests the crack growth rate is slow. In region II, the increased number of grooves indicates faster but steady crack growth. At high magnification, the striation pattern can be observed, which results from the plastic blunting and re-sharpening of the crack tip under cyclic loading. Once the crack reaches a critical size, fast fracture occurs. In region III, a dimpled rupture becomes dominant as a result of microvoid nucleation, growth, and coalescence during final failure.

We proceed to identify the fatigue crack initiation sites for the 7 specimens under study. All 63 samples tested in this work demonstrate surface-initiated fracture processes, which confirms surface roughness governs the fatigue performance of net-shape AM Ti-6Al-4V [65,16]. Based on linear elastic fracture mechanics, an arbitrarily shaped surface defect exhibit a higher geometrical factor Y (0.65) as compared to an internal defect (0.50) [66,67]. This indicates for defects of the same size, a higher stress intensity factor ΔK can be induced by a surface defect than an internal defect following

$$\Delta K = Y \Delta\sigma \sqrt{\pi \sqrt{A_P}} \tag{3}$$

where $\Delta\sigma$ is the applied stress range and $\sqrt{A_P}$ is the square root of the projection area of a defect perpendicular to the load direction.

Furthermore, when the build orientation is below 30°, all the cracks are initiated from the downward-facing surfaces since the surface roughness of the downward-facing surface is at least 90% higher than that of the otherward-facing surface. The larger defects on the downward-facing surface with higher stress intensity factors are more prone to

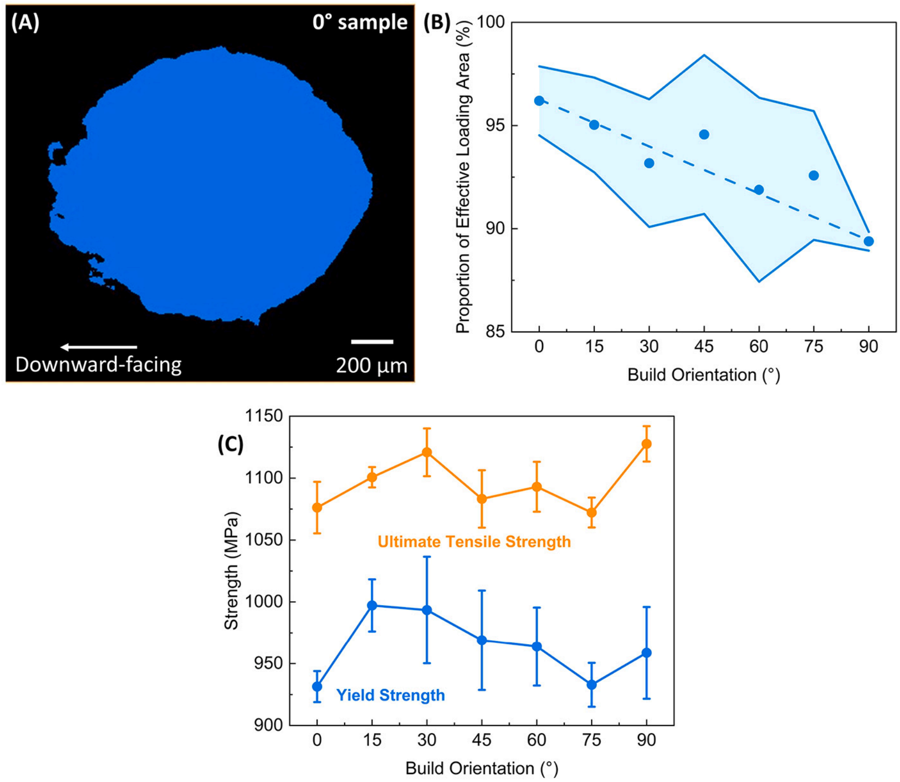

Fig. 8. (A) A segmented cross-sectional XCT slice of a 0° sample. (B) Proportion of effective loading area ± 1 standard deviation vs. build orientation of the 7 specimens under study. (C) Corrected values of yield strength and ultimate tensile strength as a function of the build orientation. Error bars represent the standard deviation from 3 repetitions.

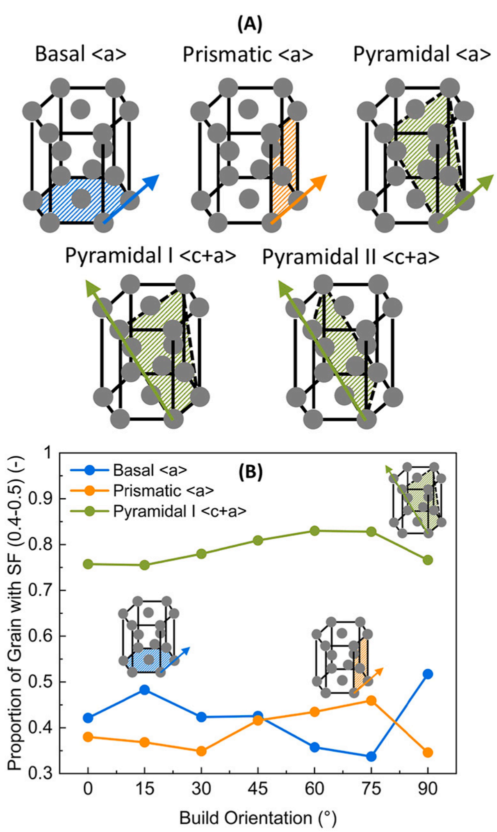

Fig. 9. (A) Schematic illustration of the slip systems in Ti-6Al-4V. (B) Schmid factors of basal ⟨a⟩, prismatic ⟨a⟩, and pyramidal I ⟨c+a⟩ slip systems as a function of the build orientation.

crack initiation during the fracture process. As the build orientation increases to 45° or above, defects on the otherward-facing surface start to serve as fatigue crack initiation sites since the differences in surface quality between the otherward-facing and downward-facing surfaces become smaller, and the differences in stress intensity factors given by the defects on the otherward-facing and downward-facing surfaces also become smaller. However, in most of the samples, the initiation process still starts from the downward-facing surfaces. When the build orientation is 75°, cracks are initiated from otherward-facing surfaces in 8 out of 9 samples owing to the relatively homogeneous surface roughness across the sample surface.

The presence of porosity can increase the stress concentration and degrade the fatigue performance even when the cracks are initiated from surface defects [16,52,68]. The stress distribution around a spherical pore perpendicular to the load direction is given following Kirsch's Solution [69]:

$$
\begin{aligned}
\sigma_{rr} &= \frac{3\sigma}{2}\left(\left(\frac{r}{d}\right)^2 - \left(\frac{r}{d}\right)^4\right) \\
\sigma_{\Theta\Theta} &= \sigma\left(1 + 2\left(\frac{r}{d}\right)^2\right) \\
\tau_{r\Theta} &= 0
\end{aligned}
\tag{4}
$$

where σ is the applied stress, r is the radius of the pore, and d is the distance from the pore center. This indicates the maximum principal stress is 3 times the applied stress σ at the pore edge. However, it reduces to $\frac{11}{9}\sigma$ at a distance of 1 pore diameter from the pore edge, which is close to the far field stress σ. Hence, we define a pore cluster as near the initiation site when it's no more than 1 diameter away from the site. Results are shown in Fig. 11(A). Clearly, when the build orientation is 45° or below, no pore can be observed close to the fatigue initiation site for the following two reasons. (1) The poor quality of the surface, especially the downward-facing surface, results in a high stress intensity factor governing the failure process. (2) Very few pores can be found in the specimens with build orientations of 30° or below. At a build

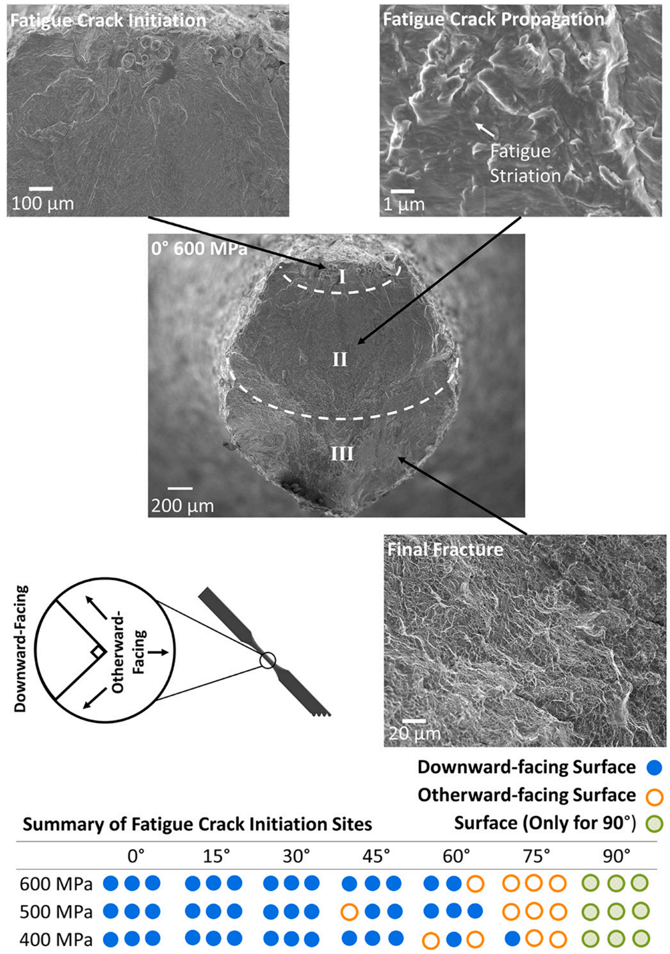

Fig. 10. Summary of fatigue crack initiation sites for the 7 specimens under study.

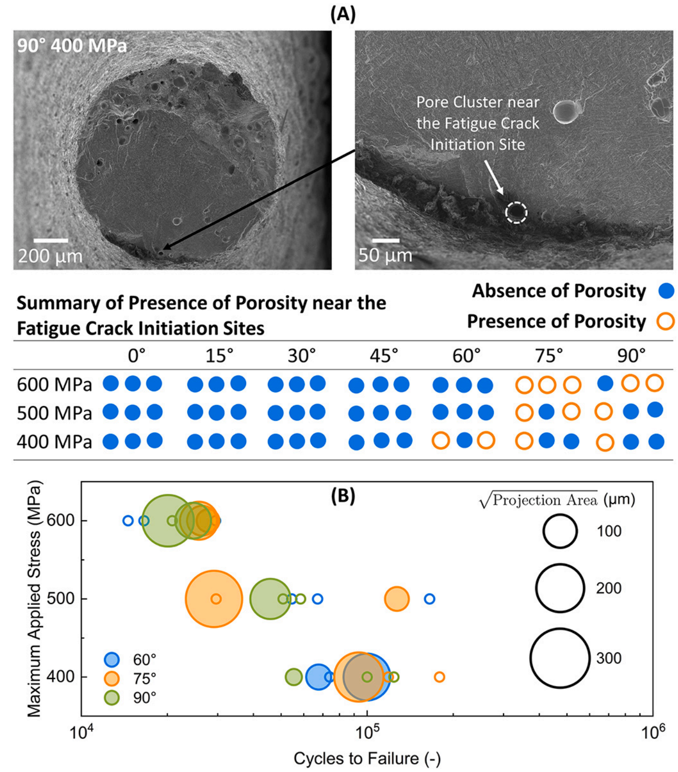

Fig. 11. (A) Summary of presence of porosity near the fatigue crack initiation sites for all the tested samples. (B) $\sqrt{A_P}$ of the pore cluster for the 60°, 75°, and 90° samples.

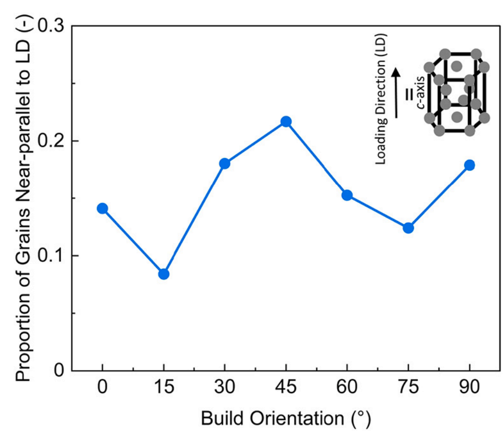

Fig. 12. Fraction of grains with c-axes near-parallel (0°-10°) to the loading direction as a function of the build orientation.

orientation of 60° or above, pores start to facilitate the initiation process owing to the lower surface roughness and higher porosity levels.

It is critical to note that the fracture processes described above are only valid when the specimens are tested at room temperature in air. The failure process may vary under different environmental conditions.

4.3. Rationalization of the variation in fatigue properties

On the basis of the results presented above, the orientation dependency of the fatigue properties can be rationalized. Having surface defects as the initiation sites confirms that at all applied stresses, as the build orientation increases from 0° to 60°, the increase in fatigue life results from the reduction in surface roughness of the downward-facing surface. At 75°, the low surface roughness of the otherward-facing surface gives rise to the optimal fatigue resistance of the specimen. When the samples are built vertically, their surface quality and porosity level are comparable to those of the 75° specimen but a reduction in fatigue life can be observed. This can be explained by the dominance of basal slip activity in Ti-6Al-4V alloys under cyclic loading [70,63,71]. Based on Stroh's theory [72], the fatigue crack formation along the basal planes results from the restricted slip on this plane in the hcp crystal. The slip activity of the surrounding soft grains would induce a transfer of stress to grains with hard α orientations, thus introducing additional tensile stress, which leads to failure along the basal plane. Moreover, since the applied stress is well below the yield strength, the elastic anisotropy of the hcp crystal can also contribute to inhomogeneity of the stress state. The stiffness of the α phase is the greatest when the load direction is parallel to the c-axis. Compatibility of deformation with surrounding grains of different crystallographic orientations dictates that for a given applied load, these grains will support the highest tensile stresses in the material [73]. Hence, even though the prismatic $\langle a \rangle$ slip system has a lower τ_c value, it is the stresses normal to the basal planes that govern the crack formation under cyclic loading [70,63,71]. This process is expected in all the L-PBF Ti-6Al-4V specimens since they mostly consist of the hcp crystals [71]. Here, we quantify the fraction of grains with c-axes near-parallel (0°-10°) to the loading direction as shown in Fig. 12. The lower fatigue life of the 90° specimen likely results from the higher proportion of stiff grains than the 75° specimen.

The contribution of porosity to the fatigue fracture process can give rise to a variation in fatigue life [74]. Here, the $\sqrt{\text{Projection Area}}$, $\sqrt{A_P}$, of the pore cluster near the initiation site is evaluated for every tested sample with a build orientation of 60° or above. Results are presented in Fig. 11(B). We use ○ to denote samples when no pore cluster can be observed near the initiation site. Apart from those with the absence of pore clusters, the samples with the lowest fatigue life at each applied stress are all associated with pore clusters close to the initiation sites, which confirms porosity can facilitate the surface-initiated fracture process. Hence, the maximal fatigue scatter of the 75° specimen at 500 MPa can be attributed to the large variation in the size and number of pores near the initiation sites.

On the other hand, the 45° specimen exhibits a high fatigue scatter at 500 MPa without any contribution of pore clusters to the fracture process. The difference in fatigue life results from the variation in the initiation sites. The sample with the highest cycles to failure exhibits a crack initiation site on the otherward-facing surface whereas the cracks are initiated from the downward-facing surface in the other two samples. This indicates the fatigue failure is not governed by the most critical defect but is rather a statistical process. The probability of occurrence of a number (n) of random defect clusters in an arbitrary area A can be given following the Poisson distribution [75]:

$$P(n) = \frac{e^{-\lambda A}(-\lambda A)^n}{n!} \tag{5}$$

where λ is the average defect density. When the build orientation is 45°, the average surface roughness R_a of the downward-facing surface is only 7.3 μm higher than that of the otherward-facing surface, which gives rise to a higher probability of crack initiation from the otherward-facing surface than the specimens with build orientations of 30° or below.

It is noteworthy that three tests per condition provide limited insights into the variation in fatigue properties. Yet, it offers solid evidence of the fatigue life of L-PBF Ti-6Al-4V as a function of the build orientation and gives an indication of the orientation dependency of the scatter in fatigue life, especially given the large differences in fatigue scatter between different specimens. Furthermore, the experimental results on the pores near the fatigue crack initiation sites are sufficient to explain the fatigue scatter behaviour and can serve as the foundation for the prediction of the fatigue life of L-PBF Ti-6Al-4V.

5. Summary and conclusions

In this study, orientation effects that influence the fatigue behaviour of Ti-6Al-4V components produced by laser powder bed fusion has been explained by means of systematic mechanical testing, high-resolution electron microscopy, and X-ray computed tomography. Seven different build orientations have been considered. The following specific conclusions can be drawn from this work:

- Dynamic fatigue tests reveal the specimen built at 75° to the build plate demonstrate the optimal fatigue resistance. An increase in fatigue life with the build orientation from 0° and 75° has been confirmed owing to the improved surface quality. The lower fatigue life of the 90° specimen may result from the large proportion of grains near-parallel to the loading direction.
- Below 30°, the fatigue cracks are initiated from the downward-facing surface for all the cases. The $\geq$ 90% higher R_a of the downward-facing surface contributes to this effect. Above 45°, defects on the otherward-facing surface start to serve as the fatigue crack initiation sites as a result of the smaller difference in R_a between downward-facing and otherward-facing surfaces.
- Pore clusters can facilitate the surface-initiated fatigue fracture process, whose role can be explained using Kirsch's Solution for the elastic stress state in the vicinity of a pore. The large difference in pore sizes and number density near the initiation sites gives rise to the maximal fatigue scatter of the 75° specimen at 500 MPa. The statistical nature of the failure process is also revealed by the variation in the initiation site of the 45° specimen, which leads to high fatigue scatter.

CRediT authorship contribution statement

Jieming S. Zhang: Writing – original draft, Investigation, Conceptualization. **Yun Deng:** Writing – review & editing, Investigation. **Huifang Liu:** Investigation. **Yuanbo T. Tang:** Investigation. **Andrew Lui:** Investigation. **Patrick S. Grant:** Investigation. **Enrique Alabort:** Funding acquisition. **Roger C. Reed:** Writing – review & editing, Supervision, Conceptualization. **Alan C.F. Cocks:** Writing – review & editing, Supervision, Conceptualization.

Declaration of competing interest

The authors declare that they have no known competing financial interests or personal relationships that could have appeared to influence the work reported in this paper.

Acknowledgements

The authors are grateful for the funding from Alloyed Ltd. and Innovate UK 43749. Helpful comments from Dr. Joseph N. Ghoussoub and Prof. D. Graham McCartney of University of Oxford are acknowledged.

Appendix A. Supplementary material

Supplementary material related to this article can be found online at https://doi.org/10.1016/j.matdes.2024.113485.

Data availability

Data will be made available on request.

References

[1] D. Gu, X. Shi, R. Poprawe, D.L. Bourell, R. Setchi, J. Zhu, Material-structure-performance integrated laser-metal additive manufacturing, Science 372 (6545) (2021), https://doi.org/10.1126/science.abg1487.
[2] T. DebRoy, H.L. Wei, J.S. Zuback, T. Mukherjee, J.W. Elmer, J.O. Milewski, A.M. Beese, A. Wilson-Heid, A. De, W. Zhang, Additive manufacturing of metallic components – process, structure and properties, Prog. Mater. Sci. 92 (2018) 112–224, https://doi.org/10.1016/j.pmatsci.2017.10.001.
[3] D. Zhang, D. Qiu, M.A. Gibson, Y. Zheng, H.L. Fraser, D.H. StJohn, M.A. Easton, Additive manufacturing of ultrafine-grained high-strength titanium alloys, Nature 576 (7785) (2019) 91–95, https://doi.org/10.1038/s41586-019-1783-1.
[4] M.S. Pham, C. Liu, I. Todd, J. Lertthanasarn, Damage-tolerant architected materials inspired by crystal microstructure, Nature 565 (7739) (2019) 305–311, https://doi.org/10.1038/s41586-018-0850-3.
[5] D. Barba, E. Alabort, R.C. Reed, Synthetic bone: design by additive manufacturing, Acta Biomater. 97 (2019) 637–656, https://doi.org/10.1016/j.actbio.2019.07.049.
[6] X. Zheng, H. Lee, T.H. Weisgraber, M. Shusteff, J. DeOtte, E.B. Duoss, J.D. Kuntz, M.M. Biener, Q. Ge, J.A. Jackson, S.O. Kucheyev, N.X. Fang, C.M. Spadaccini, Ultralight, ultrastiff mechanical metamaterials, Science 344 (6190) (2014) 1373–1377, https://doi.org/10.1126/science.1252291.
[7] B.E. Carroll, T.A. Palmer, A.M. Beese, Anisotropic tensile behavior of Ti-6Al-4V components fabricated with directed energy deposition additive manufacturing, Acta Mater. 87 (2015) 309–320, https://doi.org/10.1016/j.actamat.2014.12.054.
[8] S. Ren, Y. Chen, T. Liu, X. Qu, Effect of build orientation on mechanical properties and microstructure of Ti-6Al-4V manufactured by selective laser melting, Metall. Mater. Trans. A, Phys. Metall. Mater. Sci. 50 (9) (2019) 4388–4409, https://doi.org/10.1007/s11661-019-05322-w.
[9] L.Y. Chen, S.X. Liang, Y. Liu, L.C. Zhang, Additive manufacturing of metallic lattice structures: unconstrained design, accurate fabrication, fascinated performances, and challenges, Mater. Sci. Eng., R Rep. 146 (August) (2021) 100648, https://doi.org/10.1016/j.mser.2021.100648.
[10] D. Barba, C. Alabort, Y.T. Tang, M.J. Viscasillas, R.C. Reed, E. Alabort, On the size and orientation effect in additive manufactured Ti-6Al-4V, Mater. Des. 186 (2020) 108235, https://doi.org/10.1016/j.matdes.2019.108235.
[11] G. Shanbhag, E. Wheat, S. Moylan, M. Vlasea, Effect of specimen geometry and orientation on tensile properties of Ti-6Al-4V manufactured by electron beam powder bed fusion, Addit. Manuf. 48 (PA) (2021) 102366, https://doi.org/10.1016/j.addma.2021.102366.
[12] T.H. Becker, P. Kumar, U. Ramamurty, Fracture and fatigue in additively manufactured metals, Acta Mater. 219 (2021) 117240, https://doi.org/10.1016/j.actamat.2021.117240.

[13] M. Benedetti, A. du Plessis, R.O. Ritchie, M. Dallago, S.M. Razavi, F. Berto, Architected cellular materials: a review on their mechanical properties towards fatigue-tolerant design and fabrication, Mater. Sci. Eng., R Rep. 144 (January) (2021) 100606, https://doi.org/10.1016/j.mser.2021.100606.
[14] P. Kumar, U. Ramamurty, High cycle fatigue in selective laser melted Ti-6Al-4V, Acta Mater. 194 (2020) 305–320, https://doi.org/10.1016/j.actamat.2020.05.041.
[15] P. Kumar, O. Prakash, U. Ramamurty, Micro-and meso-structures and their influence on mechanical properties of selectively laser melted Ti-6Al-4V, Acta Mater. 154 (2018) 246–260, https://doi.org/10.1016/j.actamat.2018.05.044.
[16] J.S. Zhang, Y.T. Tang, R. Jin, A. Lui, P.S. Grant, E. Alabort, A.C.F. Cocks, R.C. Reed, On the size-dependent fatigue behaviour of laser powder bed fusion Ti-6Al-4V, Addit. Manuf. 79 (2024).
[17] S. Liu, Y.C. Shin, Additive manufacturing of Ti6Al4V alloy: a review, Mater. Des. 164 (2019) 107552, https://doi.org/10.1016/j.matdes.2018.107552.
[18] Y. Zhai, H. Galarraga, D.A. Lados, Microstructure, static properties, and fatigue crack growth mechanisms in Ti-6Al-4V fabricated by additive manufacturing: LENS and EBM, Eng. Fail. Anal. 69 (2016) 3–14, https://doi.org/10.1016/j.engfailanal.2016.05.036.
[19] L. Thijs, F. Verhaeghe, T. Craeghs, J.V. Humbeeck, J.P. Kruth, A study of the microstructural evolution during selective laser melting of Ti-6Al-4V, Acta Mater. 58 (9) (2010) 3303–3312, https://doi.org/10.1016/j.actamat.2010.02.004.
[20] Y. Hu, H. Chen, X. Jia, X. Liang, J. Lei, Heat treatment of titanium manufactured by selective laser melting: microstructure and tensile properties, J. Mater. Res. Technol. 18 (2022) 245–254, https://doi.org/10.1016/j.jmrt.2022.02.106.
[21] D. Herzog, V. Seyda, E. Wycisk, C. Emmelmann, Additive manufacturing of metals, Acta Mater. 117 (2016) 371–392, https://doi.org/10.1016/j.actamat.2016.07.019.
[22] S. Leuders, M. Thöne, A. Riemer, T. Niendorf, T. Tröster, H.A. Richard, H.J. Maier, On the mechanical behaviour of titanium alloy TiAl6V4 manufactured by selective laser melting: fatigue resistance and crack growth performance, Int. J. Fatigue 48 (2013) 300–307, https://doi.org/10.1016/j.ijfatigue.2012.11.011.
[23] Z.H. Jiao, R.D. Xu, H.C. Yu, X.R. Wu, Evaluation on tensile and fatigue crack growth performances of Ti6Al4V alloy produced by selective laser melting, Proc. Struct. Integr. 7 (2017) 124–132, https://doi.org/10.1016/j.prostr.2017.11.069.
[24] K.F. Walker, Q. Liu, M. Brandt, Evaluation of fatigue crack propagation behaviour in Ti-6Al-4V manufactured by selective laser melting, Int. J. Fatigue 104 (2017) 302–308, https://doi.org/10.1016/j.ijfatigue.2017.07.014.
[25] R. Molaei, A. Fatemi, N. Phan, Significance of hot isostatic pressing (HIP) on multiaxial deformation and fatigue behaviors of additive manufactured Ti-6Al-4V including build orientation and surface roughness effects, Int. J. Fatigue 117 (April) (2018) 352–370, https://doi.org/10.1016/j.ijfatigue.2018.07.035.
[26] G. Qian, Y. Li, D.S. Paolino, A. Tridello, F. Berto, Y. Hong, Very-high-cycle fatigue behavior of Ti-6Al-4V manufactured by selective laser melting: effect of build orientation, Int. J. Fatigue 136 (March) (2020) 105628, https://doi.org/10.1016/j.ijfatigue.2020.105628.
[27] P. Edwards, M. Ramulu, Fatigue performance evaluation of selective laser melted Ti-6Al-4V, Mater. Sci. Eng. A 598 (2014) 327–337, https://doi.org/10.1016/j.msea.2014.01.041.
[28] G. Nicoletto, Anisotropic high cycle fatigue behavior of Ti–6Al–4V obtained by powder bed laser fusion, Int. J. Fatigue 94 (2017) 255–262, https://doi.org/10.1016/j.ijfatigue.2016.04.032.
[29] W. Sun, Y. Ma, W. Huang, W. Zhang, X. Qian, Effects of build direction on tensile and fatigue performance of selective laser melting Ti6Al4V titanium alloy, Int. J. Fatigue 130 (June 2019) (2020), https://doi.org/10.1016/j.ijfatigue.2019.105260.
[30] A. Cutolo, C. Elangeswaran, G.K. Muralidharan, B. Van Hooreweder, On the role of building orientation and surface post-processes on the fatigue life of Ti-6Al-4V coupons manufactured by laser powder bed fusion, Mater. Sci. Eng. A 840 (January) (2022) 142747, https://doi.org/10.1016/j.msea.2022.142747.
[31] E. Alabort, Y.T. Tang, D. Barba, R.C. Reed, Alloys-by-design: a low-modulus titanium alloy for additively manufactured biomedical implants, Acta Mater. 229 (2022), https://doi.org/10.1016/j.actamat.2022.117749.
[32] A. Charles, A. Elkaseer, U. Paggi, L. Thijs, V. Hagenmeyer, S. Scholz, Down-facing surfaces in laser powder bed fusion of Ti6Al4V: effect of dross formation on dimensional accuracy and surface texture, Addit. Manuf. 46 (February) (2021) 102148, https://doi.org/10.1016/j.addma.2021.102148.
[33] A. Charles, M. Bayat, A. Elkaseer, L. Thijs, J. Henri, S. Scholz, Elucidation of dross formation in laser powder bed fusion at down-facing surfaces: phenomenon-oriented multiphysics simulation and experimental validation, Addit. Manuf. 50 (December 2021) (2022) 102551, https://doi.org/10.1016/j.addma.2021.102551.
[34] E. Maire, P.J. Withers, E. Maire, P.J. Withers, Quantitative X-ray tomography, Int. Mater. Rev. 59 (1) (2014) 1–43, https://doi.org/10.1179/1743280413Y.0000000023.
[35] N. Otsu, A threshold selection method from gray-level histograms, IEEE Trans. Syst. Man Cybern. 9 (1) (1979) 62–66.
[36] A. Moridi, A.G. Demir, L. Caprio, A.J. Hart, B. Previtali, B.M. Colosimo, Deformation and failure mechanisms of Ti–6Al–4V as built by selective laser melting, Mater. Sci. Eng. A 768 (July) (2019), https://doi.org/10.1016/j.msea.2019.138456.
[37] P. Li, D.H. Warner, J.W. Pegues, M.D. Roach, N. Shamsaei, N. Phan, Towards predicting differences in fatigue performance of laser powder bed fused Ti-6Al-4V coupons from the same build, Int. J. Fatigue 126 (April) (2019) 284–296, https://doi.org/10.1016/j.ijfatigue.2019.05.004.
[38] Z. Zou, M. Simonelli, J. Katrib, G. Dimitrakis, R. Hague, Microstructure and tensile properties of additive manufactured Ti-6Al-4V with refined prior-β grain structure obtained by rapid heat treatment, Mater. Sci. Eng. A 814 (November 2020) (2021) 141271, https://doi.org/10.1016/j.msea.2021.141271.
[39] C. Leyens, M. Peters, Titanium and titanium alloys, https://doi.org/10.1007/978-3-319-69743-7_7, 2003.
[40] H. Beladi, Q. Chao, G.S. Rohrer, Variant selection and intervariant crystallographic planes distribution in martensite in a Ti-6Al-4V alloy, Acta Mater. 80 (2014) 478–489, https://doi.org/10.1016/j.actamat.2014.06.064.
[41] K. Yamanaka, W. Saito, M. Mori, H. Matsumoto, A. Chiba, Preparation of weak-textured commercially pure titanium by electron beam melting, Addit. Manuf. 8 (2015) 105–109, https://doi.org/10.1016/j.addma.2015.09.007.
[42] X.P. Li, J. Van Humbeeck, J.P. Kruth, Selective laser melting of weak-textured commercially pure titanium with high strength and ductility: a study from laser power perspective, Mater. Des. 116 (2017) 352–358, https://doi.org/10.1016/j.matdes.2016.12.019.
[43] B. Ahuja, M. Karg, K.Y. Nagulin, M. Schmidt, Fabrication and characterization of high strength Al-Cu alloys processed using Laser Beam Melting in metal powder bed, Phys. Proc. 56 (C) (2014) 135–146, https://doi.org/10.1016/j.phpro.2014.08.156.
[44] D. Koutny, D. Palousek, L. Pantelejev, C. Hoeller, R. Pichler, L. Tesicky, J. Kaiser, Influence of scanning strategies on processing of aluminum alloy EN AW 2618 using selective laser melting, Materials 11 (2) (2018), https://doi.org/10.3390/ma11020298.
[45] C.L. Smithson, T. Davis, T.W. Nelson, N.B. Crane, Effect of support structures and surface angles on near-surface porosity in laser powder bed fusion, J. Manuf. Process. 94 (February) (2023) 328–337, https://doi.org/10.1016/j.jmapro.2023.03.065.
[46] A. Çelik, E. Tekoğlu, E. Yasa, M.Å. Sönmez, Contact-free support structures for the direct metal laser melting process, Materials 15 (11) (2022), https://doi.org/10.3390/ma15113765.
[47] U. Paggi, L. Thijs, B.V. Hooreweder, Implementation of contactless supports for industrially relevant additively manufactured parts in metal, Addit. Manuf. Lett. 3 (June) (2022) 100095, https://doi.org/10.1016/j.addlet.2022.100095.
[48] J. Damon, S. Dietrich, F. Vollert, J. Gibmeier, V. Schulze, Process dependent porosity and the in fl uence of shot peening on porosity morphology regarding selective laser melted AlSi10Mg parts, Addit. Manuf. 20 (2018) 77–89, https://doi.org/10.1016/j.addma.2018.01.001.
[49] A.D. Plessis, S.G. le Roux, Standardized X-ray tomography testing of additively manufactured parts: a round robin test, Addit. Manuf. 24 (2018) 125–136, https://doi.org/10.1016/j.addma.2018.09.014.
[50] A.D. Plessis, D. Glaser, S. Africa, N.R. Mathe, S. Africa, Pore closure effect of laser shock peening of additively manufactured AlSi10Mg, 3D Print. Addit. Manuf. 6 (5) (2019) 245–252, https://doi.org/10.1089/3dp.2019.0064.
[51] Y. Murakami, M. Endo, Effects of defects, inclusions and inhomogeneities on fatigue strength, Int. J. Fatigue 16 (3) (1994) 163–182, https://doi.org/10.1016/0142-1123(94)90001-9.
[52] S. Tammas-Williams, P.J. Withers, I. Todd, P.B. Prangnell, The influence of porosity on fatigue crack initiation in additively manufactured titanium components, Sci. Rep. 7 (1) (2017) 1–13, https://doi.org/10.1038/s41598-017-06504-5.
[53] D. El Khoukhi, F. Morel, N. Saintier, D. Bellett, P. Osmond, V.D. Le, Probabilistic modeling of the size effect and scatter in High Cycle Fatigue using a Monte-Carlo approach: role of the defect population in cast aluminum alloys, Int. J. Fatigue 147 (January) (2021) 106177, https://doi.org/10.1016/j.ijfatigue.2021.106177.
[54] Y. Murakami, 18 - Additive manufacturing: effects of defects, in: Y. Murakami (Ed.), Metal Fatigue, second edition, Academic Press, 2019, pp. 453–483.
[55] A. Nouri, A. Rohani Shirvan, Y. Li, C. Wen, Additive manufacturing of metallic and polymeric load-bearing biomaterials using laser powder bed fusion: a review, J. Mater. Sci. Technol. 94 (2021) 196–215, https://doi.org/10.1016/j.jmst.2021.03.058.
[56] E.O. Olakanmi, R.F. Cochrane, K.W. Dalgarno, A review on selective laser sintering/melting (SLS/SLM) of aluminium alloy powders: processing, microstructure, and properties, Prog. Mater. Sci. 74 (2015) 401–477, https://doi.org/10.1016/j.pmatsci.2015.03.002.
[57] D. Zhang, L. Wang, H. Zhang, A. Maldar, G. Zhu, W. Chen, J.S. Park, J. Wang, X. Zeng, Effect of heat treatment on the tensile behavior of selective laser melted Ti-6Al-4V by in situ X-ray characterization, Acta Mater. 189 (2020) 93–104, https://doi.org/10.1016/j.actamat.2020.03.003.
[58] S. Hémery, A. Nait-Ali, P. Villechaise, Combination of in-situ SEM tensile test and FFT-based crystal elasticity simulations of Ti-6Al-4V for an improved description of the onset of plastic slip, Mech. Mater. 109 (2017) 1–10, https://doi.org/10.1016/j.mechmat.2017.03.013.
[59] V. Hasija, S. Ghosh, M.J. Mills, D.S. Joseph, Deformation and creep modeling in polycrystalline Ti-6Al alloys, Acta Mater. 51 (15) (2003) 4533–4549, https://doi.org/10.1016/S1359-6454(03)00289-1.
[60] I. Bantounas, D. Dye, T.C. Lindley, The effect of grain orientation on fracture morphology during high-cycle fatigue of Ti-6Al-4V, Acta Mater. 57 (12) (2009) 3584–3595, https://doi.org/10.1016/j.actamat.2009.04.018.
[61] R. Zhao, C. Chen, W. Wang, T. Cao, S. Shuai, S. Xu, T. Hu, H. Liao, J. Wang, Z. Ren, On the role of volumetric energy density in the microstructure and mechanical properties of laser powder bed fusion Ti-6Al-4V alloy, Addit. Manuf. 51 (September 2021) (2022) 102605, https://doi.org/10.1016/j.addma.2022.102605.

[62] J.C. Williams, R.G. Baggerly, N.E. Paton, Deformation behavior of HCP Ti-Al alloy single crystals, Metall. Mater. Trans. A, Phys. Metall. Mater. Sci. 33 (13) (2002) 837–850, https://doi.org/10.1007/s11661-002-1016-2.

[63] F. Bridier, D.L. McDowell, P. Villechaise, J. Mendez, Crystal plasticity modeling of slip activity in Ti-6Al-4V under high cycle fatigue loading, Int. J. Plast. 25 (6) (2009) 1066–1082, https://doi.org/10.1016/j.ijplas.2008.08.004.

[64] T. Mukai, M. Yamanoi, H. Watanabe, K. Higashi, Ductility enhancement in AZ31 magnesium alloy by controlling its grain structure, Scr. Mater. 45 (1) (2001) 89–94, https://doi.org/10.1016/S1359-6462(01)00996-4.

[65] P. Li, D.H. Warner, A. Fatemi, N. Phan, Critical assessment of the fatigue performance of additively manufactured Ti-6Al-4V and perspective for future research, Int. J. Fatigue 85 (2016) 130–143, https://doi.org/10.1016/j.ijfatigue.2015.12.003.

[66] U. Karr, B. Schönbauer, M. Fitzka, E. Tamura, Y. Sandaiji, S. Murakami, H. Mayer, Inclusion initiated fracture under cyclic torsion very high cycle fatigue at different load ratios, Int. J. Fatigue 122 (November 2018) (2019) 199–207, https://doi.org/10.1016/j.ijfatigue.2019.01.015.

[67] S.C. Wu, Z. Song, G.Z. Kang, Y.N. Hu, Y.N. Fu, The Kitagawa-Takahashi fatigue diagram to hybrid welded AA7050 joints via synchrotron X-ray tomography, Int. J. Fatigue 125 (March) (2019) 210–221, https://doi.org/10.1016/j.ijfatigue.2019.04.002.

[68] Z. Xu, W. Wen, T. Zhai, Effects of pore position in depth on stress/strain concentration and fatigue crack initiation, Metall. Mater. Trans. A, Phys. Metall. Mater. Sci. 43 (8) (2012) 2763–2770, https://doi.org/10.1007/s11661-011-0947-x.

[69] P. Jussila, Analytical Solutions of the Mechanical Behaviour of Rock with Applications to a Repository for Spent Nuclear Fuel, October 1997.

[70] F. Bridier, P. Villechaise, J. Mendez, Slip and fatigue crack formation processes in an α/β titanium alloy in relation to crystallographic texture on different scales, Acta Mater. 56 (15) (2008) 3951–3962, https://doi.org/10.1016/j.actamat.2008.04.036.

[71] D. Banerjee, J.C. Williams, Perspectives on titanium science and technology, Acta Mater. 61 (3) (2013) 844–879, https://doi.org/10.1016/j.actamat.2012.10.043.

[72] A.N. Stroh, A theory of the fracture of metals, vol. 6, https://doi.org/10.1080/00018735700101406, 1957.

[73] M. Hayes, Connexions between the moduli for anistropic elastic materials, J. Elast. 2 (2) (1972) 135–141, https://doi.org/10.1007/BF00046063.

[74] N. Macallister, T.H. Becker, Fatigue life estimation of additively manufactured Ti-6Al-4V: sensitivity, scatter and defect description in Damage-tolerant models, Acta Mater. 237 (2022) 118189, https://doi.org/10.1016/j.actamat.2022.118189.

[75] K.S. Ravi Chandran, Duality of fatigue failures of materials caused by Poisson defect statistics of competing failure modes, Nat. Mater. 4 (4) (2005) 303–308, https://doi.org/10.1051/nmat1351.